International Journal of Heat and Technology
Vol. 42, No. 4, August, 2024, pp. 1484-1494
Journal homepage: http://iieta.org/journals/ijht

Drag Behavior of 25° Ahmed Body Effect by Deflector Length and Angles

Pham Van Duy[1], Tran The Hung[2*], Le Dinh Anh[3], Trinh Xuan Long[2], Naseeb Ahmed Siddiqui[4]

[1] School of Mechanical Engineering, Hanoi University of Science and Technology, Hai Ba Trung 11615, Vietnam
[2] Faculty of Aerospace Engineering, Le Quy Don Technical University, Bac Tu Liem 100000, Vietnam
[3] VNU-University of Engineering and Technology, Vietnam National University, Caugiay 100000, Vietnam
[4] Engineering Cluster, Singapore Institute of Technology, Singapore, Singapore

Corresponding Author Email: thehungmfti@gmail.com

https://doi.org/10.18280/ijht.420438

Received: 13 June 2024
Revised: 15 August 2024
Accepted: 27 August 2024
Available online: 31 August 2024

Keywords:
Ahmed body, deflector length, skin friction, separation bubble, longitudinal vortex

ABSTRACT

This study investigates the influence of deflector length on the aerodynamic drag and flow characteristics of a standard 25° Ahmed body by a numerical approach. Two class of deflector was selected for investigation to elucidate the impact of angles parameter on both drag and flow characteristics. The first class has a fixed length of 9% of the slant's length and spanning angles from -25° to 25°. The second one has length varying from 0% to 100% of the slant's length deflectors and angles from -5° to 5°. Reynolds Average Navier-Stokes equations with the generalized *k-ω* (GEKO) model were selected. The numerical methods were conducted with the help of Ansys Fluent software. The numerical parameters of the model were adjusted to obtain the satisfying results of flow and drag. Numerical results were verified by experimental data at similar flow conditions. It was shown that the -5° defector allows for a reduction drag for all lengths tested with a maximum reducing drag of 19%. At the 5° deflector, 14% of the drag reduction was observed when its length is 0.3 length of the slant. For longer deflector lengths, the drag increases again. The deflector shows a good passive technique for drag reduction. However, parameters of the deflector should be carefully investigated and selected. The detailed skin-friction structure, pressure distribution, and wake flow fields relating to the drag behavior are analyzed in this study.

1. INTRODUCTION

Minimizing air resistance and enhancing the aerodynamic efficiency of vehicles have been of crucial importance recently. So far, most energy sources are from fuel foil, which creates a large quantity of dangerous emissions during the operation of the vehicles. This problem is significant in the urban area, where the population is high. Since the aerodynamic force is in direct proportion to the square of vehicles' velocity, reducing aerodynamic force is a good approach for decreasing drag on highways in comparison to using a higher powerful engine. By an estimation, reducing 50% drag results in saving 4% fuel consumption [1].

The Ahmed body, introduced by Ahmed et al., has emerged as a benchmark model for investigating the aerodynamic phenomenon of vehicles [2]. This model features an adjustable rear section allowing for variations in the slant angle, which helps to modify the surface flow and wake structure. At a slant angle of 25°, the flow around the slant is characterized by a separation bubble spreading to the midpoint of two longitudinal vortices above side edges, and a large wake flow. This large and stable structure forms a low-pressure area at the slant and contributes to a high drag level. Previous studies have extensively investigated the generation and interaction of these features to comprehend drag behavior and devise control strategies [3-7].

One of the passive control techniques, which is called deflector, added around the slant, showed a high effectiveness in drag reduction. Beaudoin and Aider [8] conducted experiments with deflectors positioned at various locations around the modified 30° Ahmed body and observed a maximum reducing drag of 25%. Their findings highlighted the crucial role of deflectors in breaking down separation bubbles and weakening longitudinal vortices above the slant. Fourrie et al. [9], added to this understanding by attaching a deflector at the leading edge of the 25° slant angle of the Ahmed body at Reynolds number Re_H=3.10×10^5 and 7.70×10^5. They identified a typical deflection with a 5° angle above the horizontal axis, beyond which both separation bubble and longitudinal vortices dissipated. Consequently, the drag of the models decreased by up to 9%. Wang et al. [10] reported a drag reduction of around 9% compared to the standard model for the model with 9% deflector length at Re_H =2.00×10^5. Note that the results by Wang et al. [10] are in contrast to the observation by Fourrie et al. [9] at 0° deflection. The discrepancies in results for that case, where Wang et al. [10] observed a reduction in drag while Fourrie et al. [9] reported the highest drag, were attributed to the influence of Reynolds number on flow fields and the drag of the model. Tran et al. [11] later categorized and analyzed these diverse outcomes. A short summary of previous studies using deflectors for drag reduction is presented in Table 1.

Table 1. Previous studies using deflectors to reduce drag

Researchers	Ahmed Body, Slant Angle	Deflector Length (%)	Investigation Methods	Reynolds Number (Re_H)	Max DR (%)
Beaudoin and Aider [8]	¼ scale, 30	9	Experiments, force, and velocities fields	3.90×10^5, 7.90×10^5	25
Fourrie et al. [9]	Standard model, 25	9	Experiments, force and velocities fields, oil flow	3.10×10^5, 7.70×10^5	9
Wang et al. [10]	½ scale, 25	4.5-13.5	Experiments, force, and velocities fields	2.40×10^5	10.9
Kim et al. [1]	Standard model, 25	60-100	Experiments, velocities fields (Automatic deflector)	2.40×10^5	19
Tian et al. [12]	Standard model, 25, 35	9	Numerical simulation	1.38×10^6	21
Raina et al. [13]	Standard model, 25	9	Numerical simulation, k-ω turbulent model	3.10×10^5, 7.70×10^5	7
Cheng et al. [14]	Standard model, 35	30	Experiments, force, and pressure	7.4×10^5	10.7
Kamaci and Kaya [15]	Standard model, 25, 35		Numerical simulation, k-ω SST	7.2×10^5	2.3
Siddiqui and Chaab [16]	Standard, 35	100	Numerical simulation, k-ω SST	7.8×10^5	14
Maine et al. [17]	Standard model, 25	9		7.9×10^5	5.8
Tran et al. [11]	7/10 scale, 25	9,18,30	Pressure tap, PIV, flow visualization (Automatic defector)	2.4×10^5	11
Tran et al. [18]	7/10 scale, 25	9	Experiments, velocities fields (Automatic deflector)	2.4×10^5	8
Current study	7/10 scale, 25	0-100	Fixed deflectors	2.4×10^5	

In terms of deflector length, Wang et al. [10] obtained a similar drag reduction at around 10% for three deflector lengths from 4.5 to 13.5%. Tran et al. [18] used automatic deflectors and obtained a maximum reduction of around 11% at 30% deflector length. Kim et al. [1], who studied the impact of long deflector lengths from 60% to 100% on the drag level of the 25° Ahmed body, observed a maximum drag reduction of around 18%. Unfortunately, Kim et al. [1] and Tran et al. [18] used automatic lifting flaps, where the lifting angle of the deflectors depends on their weight. Additionally, the fluid-structure interaction may occur and affect the aerodynamic performance of the vehicle. It can be seen that although many studies were conducted, there is a gap for short and long deflector lengths to their impact on the drag level and flow behavior of the Ahmed body. In details, the length of deflector from 13.5% to 100% and its effect on drag was not investigated for fixed deflector. Additionally, it is not clear how much the drag can be reduced in comparison to the baseline cases. Consequently, further study should be conducted to answer these questions.

Recently, the advancement of technology has elevated the significance of computational fluid dynamics as a crucial tool for addressing fluid mechanics issues. The Reynolds averaged Navier-Stokes (RANS) equations provide acceptable results while saving numerical times although the turbulent model and parameters should be carefully adjusted [19-21]. Regarding the Ahmed body, it was confirmed that although RANS and its modification methods can show a good drag and flow behavior for zero degree Ahmed body [22] and the 35° Ahmed body [16, 23, 24], the RANS simulation fails to forecast the surface flow pattern of the 25° Ahmed body [25-29]. The higher numerical scheme, such as large eddy simulation [30-33], or Lattice Boltzmann method [34] have been applied for 25° Ahmed body and show high potential in extracting flow on the slant surface. However, those numerical simulations require a large size of the mesh and numerical times, which prevents the application for a wide range of investigations. An advantage simulation model, which can simulate well the surface flow and drag trend for a wide change of flow behavior and saving numerical time should be developed for further investigation.

In this research, we enhance RANS simulation models to investigate the flow over the slant and wake of the Ahmed body across various deflector angles and lengths. The primary objective is to gain insights into how a deflector, affixed to the leading edge of the slant, influences surface flow and contributes to the drag level of the model. The second objective is to adjust parameters of numerical model to obtain high accurate results of drag and surface flow. For these purposes, we selected two class of deflectors, one with a constant length of 9% of the slant's length and spanning angles from -25° to 25°, other with length varying from 0% to 100% of the slant's length deflectors and angles from -5° to 5°. Our results indicate that the 5° deflector model shows a different drag trend to two other cases. A maximum drag reduction for that configuration is 14% at the 30% length of the slant. For -5° and 0° deflectors, the drag decreases with increasing deflector length and maximum drag reduction obtains 19%. The surface, wake flow patterns, and pressure on the slant are extracted and discussed.

2. MODEL GEOMETRY AND NUMERICAL

2.1 Model geometry and meshing

The model employed in this investigation is a scaled-down version of the Ahmed body, specifically 75% of its original size, which closely resembles the setup utilized in a prior study conducted by Tran et al. [35]. The use of the model is helpful for the validation and comparison of the results. Although the size of the model is smaller than the standard Ahmed body, the characteristics of flow are similar for Reynolds numbers higher than 2×10^4 [36]. The slant angle of 25° is selected for the study, as it was widely used due to the distinct formation of separation and longitudinal vortices. It is noteworthy that at this angle, the stability of the separation and longitudinal vortices' structure facilitates easier capture through

experiments. However, the use of RANS simulation was a challenge for the flow in previous studies. The model and its dimensions are shown in Figure 1.

The study also examines the impact of deflector angles on drag by testing various angles while maintaining a fixed length of 9% of the slant length. For this investigation, the angle of the deflector is changed from -25° (standard configuration) to 25°. Furthermore, a total of nine separate configurations were tested as well. Different deflectors with angles θ of -5°, 0, and 5° and length l from 4.5% to 100% length of the slant S were attached to the shoulder to classify the impact of length on drag and flow behavior of the model. The deflector's width matches that of the model, and its thickness is 1.5 mm, aligning with the specifications outlined in earlier investigations by Tran et al. [11, 35]. The geometry of the deflector and the definition of the deflector angle are illustrated in Figure 1.

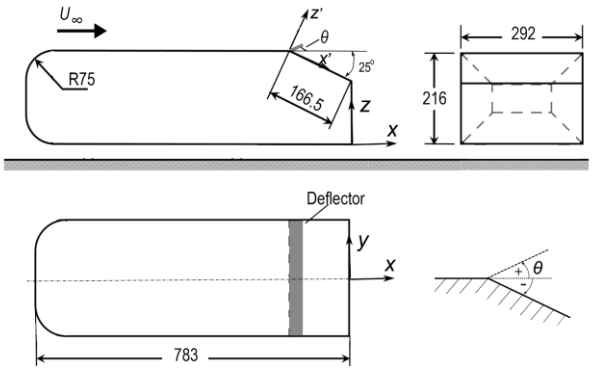

Figure 1. Numerical model and determination of deflector angles

The numerical domain has a size of 40.6H × 15H × 8H, as shown in Figure 2, to capture detailed flow structure around the model. The distance from the ground to the model is 37.5 mm. The inlet, which is at a distance 14H before the model, is chosen at velocity-inlet, and the outlet is set at pressure outlet. Other regions are chosen as wall functions. Since the velocity is low, the air density and viscosity are considered constant values in this study.

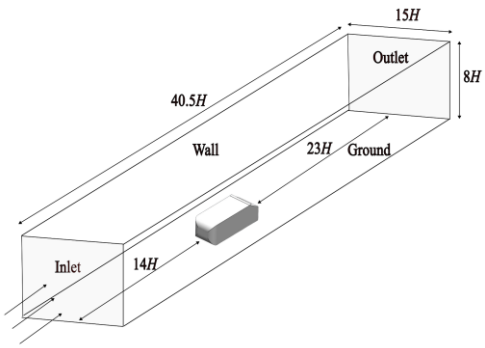

Figure 2. Numerical domain

Unstructured poly mesh is generated for the simulation. The mesh is generated by Meshing software in a copyrighted Ansys Package. Fifteen uniform layers are employed around the model to accurately capture the boundary layer. Note that the selection of mesh for different flaps is quite a challenge, particularly when the angle of the deflector is changed. To increase cell volume for capturing the correct flow phenomenon, an additional dense region is generated around the slant. The initial layer thickness of the mesh was set at 0.1 mm. Far the model, the mesh volume increases to reduce the total mesh size. Figure 3 illustrates the mesh structure surrounding the model. The maximum value of y^+ is around 2.0 for all tests in this study (Figure 3(c)).

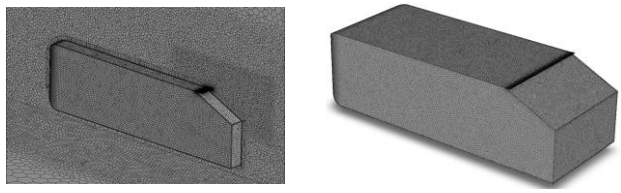

(a) Mesh around the model

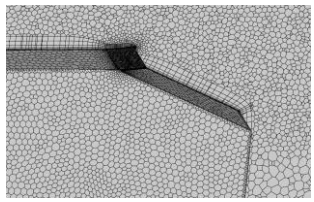

(b) Mesh around the deflector

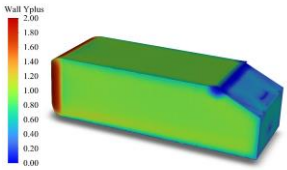

(c) Distribution of the y+ around the model

Figure 3. Mesh distribution around the model and y^+ distribution

2.2 Mesh independence study

The impact of mesh volume on the aerodynamic drag coefficient is examined to select an appropriate computational mesh. Here, the initial thickness of the mesh around the model remains the same for all cases, while the mesh at other regions is changed. The maximum coefficient y^+ also remained at around 2 for all cases. The outcome of the investigation on mesh independence is presented in Table 2. As can be seen the drag increases and becomes stable when the size of the mesh is above 2.0 million cells. The mesh with around 2.4 million cells is selected for all cases to save numerical time and accurate results. Note that the reasonable mesh size for studying flow around Ahmed body by RANS methods is around 2-3 million cells. A similar mesh size was noted by Viswanathan [23].

Table 2. Effect of mesh size on aerodynamic drag and maximum y^+ of the model

Cell Number (× 10^6)	C_D
0.494	0.370
1.087	0.334
1.363	0.323
2.362	0.320
3.919	0.320
11.001	0.320

2.3 Numerical models

As noted by Guilmineau et al. [28], RANS turbulence models can predict flow topology on slant correctly with estimating drag of less than 3% to experimental data. However, detailed flow fields on the slant are quietly different among those numerical turbulent models. Up to the present time, accurately predicting the surface characteristics, including both separation bubble and longitudinal vortice structure, for 25° Ahmed body remains a challenging task by employing the RANS approach. In this study, the numerical simulation is

conducted by using the RANS with a Generalized k-ω (GEKO) turbulence model. This model has been introduced recently, offering the flexibility to choose various parameters. It is based on a k-ω two-equations model, enabling the selection of distinct coefficients suitable for typical flow behaviors without impacting the fundamental calibrations. Within this methodology, six parameters can be modified: C_{sep} for fine-tuning separation, C_{NW} for adjusting the rates of the wall shear stress and wall heat transfer, C_{mix} for tuning shear layer flows, C_{jet} for refining jet flow results, C_{conner} for optimizing secondary flow in corners, and C_{curv} for curvature correction. The GEKO turbulent model can be expressed through turbulent kinetic energy k and the specific dissipation rate ω as below [37]:

$$\frac{\partial(\rho k)}{\partial t}+\frac{\partial(\rho u_i k)}{\partial x_i}=\frac{\partial}{\partial x_i}\left[\left(\mu+\frac{\mu_t}{\sigma_k}\right)\frac{\partial k}{\partial x_i}\right]+P_k-C_\mu\rho k\omega \quad (1)$$

$$\frac{\partial(\rho\omega)}{\partial t}+\frac{\partial(\rho u_i\omega)}{\partial x_i}=\frac{\partial}{\partial x_i}\left[\left(\mu+\frac{\mu_t}{\sigma_\omega}\right)\frac{\partial\omega}{\partial x_i}\right]+ C_{\omega1}F_1\frac{\omega}{k}P_k-C_{\omega2}F_2\rho\omega^2+\rho F_3 CD \quad (2)$$

The turbulent-viscosity v_t is calculated as below:

$$\mu_t=\rho v_t=\rho\frac{k}{\max(\omega, S/C_{Realize})} \quad (3)$$

Other terms are shown as:

$$P_k=-\tau_{ij}\frac{\partial u_i}{\partial x_j}$$

$$\tau_{ij}=2\mu_t S_{ij}-\frac{2}{3}\rho k\delta_{ij}$$

$$CD=\frac{2}{\sigma_\omega}\frac{1}{\omega}\frac{\partial k}{\partial x_j}\frac{\partial\omega}{\partial x_j}$$

$$S_{ij}=\frac{1}{2}\left(\frac{\partial u_i}{\partial x_j}+\frac{\partial u_j}{\partial x_i}\right)$$

$$S=\sqrt{2S_{ij}S_{ij}}$$

In these above equations, σ_k, σ_ω, C_μ, $C_{\omega1}$ and $C_{\omega2}$ are model constant parameters and are selected as defaulted number. The functions of F_1, F_2 and F_3 contain the constant parameters C_{sep}, C_{NW}, C_{mix}, C_{jet}, C_{conner} and C_{curv} of the GEKO model.

Note that when the above six parameters are selected as default, it becomes the turbulent model k-ω. In our initial calculation with standard parameters, the turbulent model k-ω cannot capture well the flow structure near the model. It was shown that the k-ω turbulent model overestimates flow behavior around the objects. It suggests to increasing the C_{sep} coefficient for a reliable surface low on the slant. In this study, the coefficient C_{sep} is changed from 0.70 to 2.50 to examine the flow behavior. The effect of coefficient C_{sep} on the flow and pressure coefficients at the slant of the standard 25° Ahmed body is shown in Figure 4. Here, S stands for the length of the slant. Note that when the coefficient C_{sep} equals 1.75, the turbulent model is standard k-ω. The C_{sep} = 0.7 stands for the minimum selection of the coefficient while C_{sep}=2.5 are maximum selection, which can be changed. Clearly, the coefficient C_{sep} has a strong impact on the flow while the pressure fields change little. At C_{sep}=0.7, the slant does not exhibit the formation of a separation bubble, while the default coefficient of 1.75 shows a short length of the separation, which is different from the experimental results. The coefficient of C_{sep}=2.5 shows the structure of the separation bubble with a length of 0.5H, which are close to previous experimental investigations [2, 38]. Consequently, this coefficient is selected for the simulation process. Note that two other parameters of the GEKO model, which are C_{NW} and C_{jet}, may affect strongly the results. However, initial tests in the current study indicated that the surface flow is little changed with those parameters. Consequently, those coefficients were chosen as default values. For the details, Table 3 shows the six parameters for the simulation in the current study.

Table 3. Numerical parameters of the GEKO model

Parameters	Ranges	Selection of the Current Study
C_{sep}	0.7-2.5	2.50
C_{NW}	-2.0-2.0	0.50
C_{mix}	0.0-1.0	1.00
C_{jet}	0.0-1.0	0.90
C_{conner}	0.0-1.5	1.00
C_{curv}	0.0-1.5	1.00

The COUPLED numerical scheme was used for the high accuracy of the results. The inlet velocity is set at 18 m/s for all testing cases. The Reynolds number, calculated based on the height of the model, is approximately Re_H = 2.0×10^5, falling within a comparable range to previous studies on the 25° Ahmed body, shown in Table 1. The flux type is selected as Rhie-Chow on distance base. The second order is selected for derivatives of velocities, pressure, turbulent kinetic energy, and specific dissipation rate. The residual values are specified at 10^{-6}.

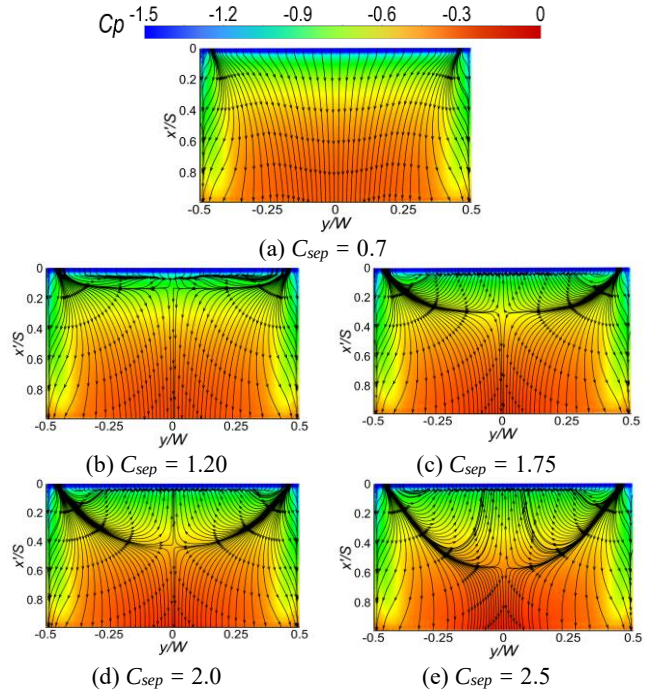

(a) C_{sep} = 0.7

(b) C_{sep} = 1.20

(c) C_{sep} = 1.75

(d) C_{sep} = 2.0

(e) C_{sep} = 2.5

Figure 4. Effect of C_{sep} on the surface flow and pressure distributions

3. RESULTS AND DISCUSSIONS

3.1 Drag and surface flow of the model with 9% deflector length for validations

Figure 5 presents the aerodynamic drag of the model with 9% deflector length at different angles. The experimental results at Re_H=3.1×10^5 by Fourrie et al. [9] were also added for comparison. It is clear that the numerical results show a similar tendency and are close to experimental data. Here, the aerodynamic drag quickly increases with flap angles up to 0°, then it suddenly decreases and the minimum drag is found for the deflector angle of 5°. The maximum difference in drag between experiments and the current simulation is around 4.8% for the deflector angle of 16°. The reduction in drag is associated with the disruption of the separation bubble and longitudinal vortices, which was reported in previous studies for similar configurations. For the deflector angles above 5°, there is a slight increase in the total drag. This trend aligns with previous findings by Tran et al. [18], despite variations in the magnitude. The observed consistency can be attributed to the influence of the initial flow conditions and the setup of the experiments. It should be noted that Tran et al. [18] used legs to support the model above the ground. However, in the current simulation, the model has no legs. Consequently, the model experiences a decrease in drag in the present investigation compared to the previous one. In comparison to the case of the 35° Ahmed body investigated by Viswanathan [23], the use of the deflector reduces drag up to a deflector angle of 25°, which is different from the case of 35°, where an increase in drag was obtained.

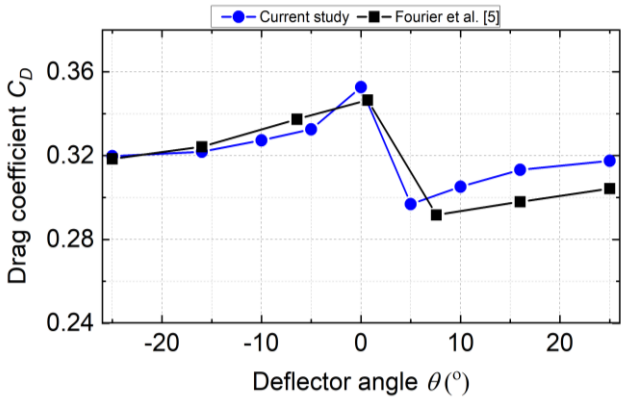

Figure 5. Drag of the model for different deflector angles

For a detailed flow structure of the numerical simulation, Figure 6 presents the surface flow at the slant superimposed on pressure coefficients for various deflector angles. In the model without deflector (Figure 6(a) - θ = -25°), a separation bubble and two longitudinal vortices are noticed, leading to the formation of a low-pressure area around the shoulder and two side edges. The length of the separation for that case is around 0.6 length of the slant surface which is similar to other studies such as Tran et al. [18]. This structure of the separation bubble and two longitudinal vortices can be obtained evidently from the Q-criterion, as illustrated later in Figure 13. This flow structure is in high agreement with the results of the previous skin-friction pattern by Tran et al. [18]. Note that previous numerical studies using RANS turbulent models failed to simulate the surface skin friction fields for the standard model. Here, the selection of the generalized GEKO turbulent model with numerical parameters is important to obtain the results. When the deflector angles increase up to 0°, the recirculation bubble becomes longer leading to widening low-pressure areas. Those could be the results of increasing drag, as shown in Figure 6. For higher deflector angles, the separation bubble disappears on the surface. Additionally, a C-type of attached flow is formed on the slant. Interestingly, secondary separation around the leading edge is evident in the skin friction fields. The pressure becomes a flat distribution, which explains the decrease in drag. This flow structure is similar to the previous findings by Tran et al. [18], who utilized luminescent oil for skin friction measurement to study surface flow. Note that although the tendency of the drag of the model with deflectors was investigated by the previous simulations [26, 30], the skin-friction streamlines were not paid attention in previous studies for 25° Ahmed body with deflectors.

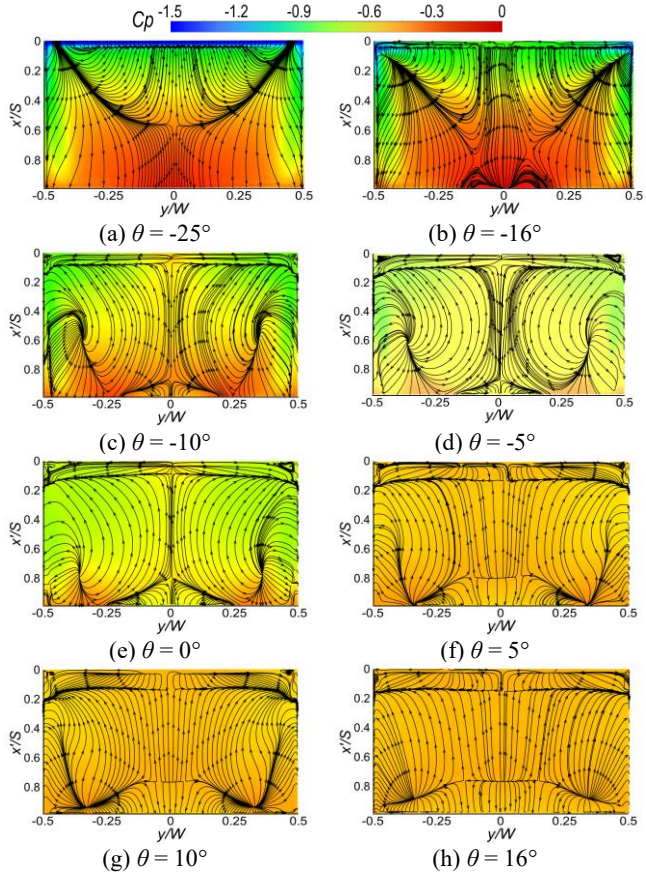

Figure 6. Skin-friction lines superimposed on pressures at the slant

Figure 7 presents the velocity on the symmetry plane for various deflector angles. In the standard scenario, a large separation occurs at the base edge and the wake is featured by a reversed flow region with a length of around 0.6-0.7*H*. This flow structure is consistent with previous experimental observations of the wake flow by both Kim et al. [1] and Tran et al. [11]. It is indicated that although the wake is not large, low-pressure areas generated at the slant contribute to large aerodynamic drag. For increasing the deflector angle up to -16°, the wake structure is little changed, except for a clearer pattern of the separation bubble. However, for deflector angles of -10° and -5°, the wake widens in the vertical direction and covers both the slant and base. The upper vortex center moves upper and close to the base surface. The length of the wake changes little, which indicates that the fully separated flow

occurs mainly only around the centerline. These results are similar for the deflector angles of 0°, which can also be witnessed from the pressure and the surface skin friction, as shown in Figure 6(d), (e). Here, the full separation flow can be observed only around the symmetry plane, while the longitudinal vortices are clearly identified at the side edges. This flow type is called a located separation, which was not taken attention, previously. For a higher deflector angle, the length of the wake highly increases with the movement of the upper center vortex far from the base. The flow is completely separated resulting in a uniform pressure distribution on the slant. A large reduction of the drag is observed for those configurations. Note that the flow on the slant with deflector was presented first in this study by the RANS method.

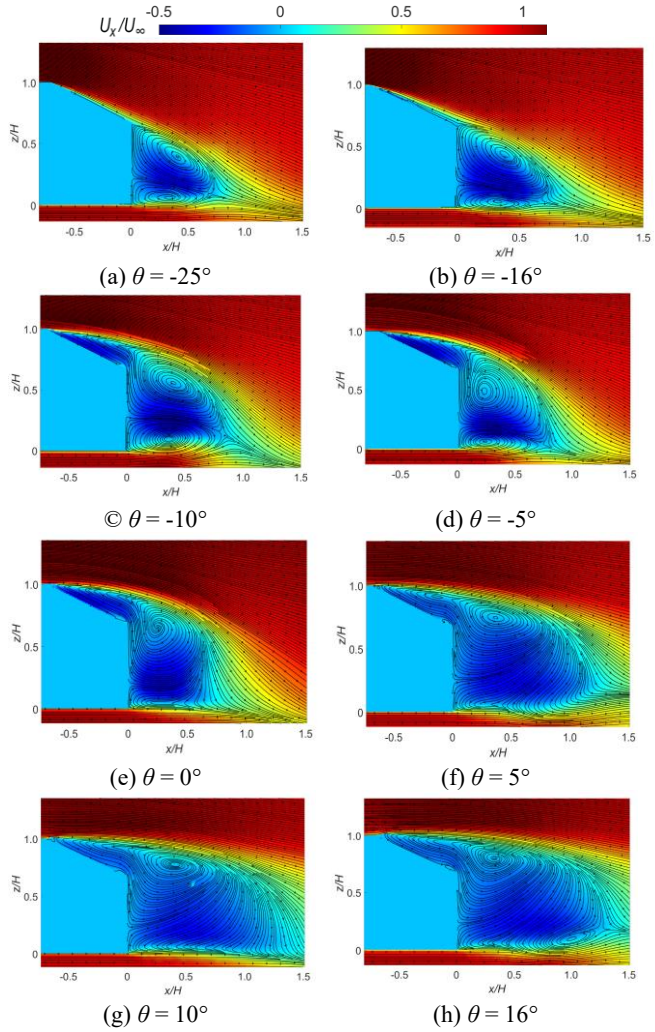

Figure 7. Streamlines superimposed to streamwise velocity on the symmetry plane

Although the flow characteristics of the model with deflector were documented previously by Fourrie et al. [9], and later by Tran et al. [18], previous studies used experimental methods and required advantageous data processing techniques for acquiring skin friction fields. In the current study, by selecting appropriate numerical parameters, detailed skin-friction fields and near-wake structure can be obtained. It was also noted that the drag and wake flow is highly modified at three angles of -5°, 0°, and 5°. Consequently, those configurations are selected for extendedly studying the impact of the deflector lengths on the drag behavior.

3.2 Deflector length effect on drag

In the next discussion, the total drag attached deflector angles of -5°, 0°, and 5 and varying lengths are extensively investigated. The numerical results are presented in Figure 8. Here, l stands for the length of the deflector. A similar drag trend for l/S < 0.5 was observed for three angles. For the standard model, drag coefficient C_D=0.32 is closed to previous observation by Tran et al. [11]. For the 5° deflector model, drag increases to 0.045 l/S, then it drops down to 0.30 l/S with a maximum drag reduction of 30%. The drag increases again for deflector length l/S > 0.4. For l/S > 0.8, only 2% of drag reduction was observed. At other cases of -5° and 0°, the tendency of the drag is similar with an increase for deflector length up to 0.09 l/S, then the drag gradually decreases for longer deflector length. However, the drag reduction is much higher for the deflector angles of -5° in comparison to that of 0°. The maximum drag reduction is observed around 19% for l/S=1.0 and the angle of -5°. The drag coefficient with minimum drag was C_D=0.26. Similar to the scenario with a 5° deflector, reducing drag for the model of 0° deflector and at l/S > 0.8 is only around 2%.

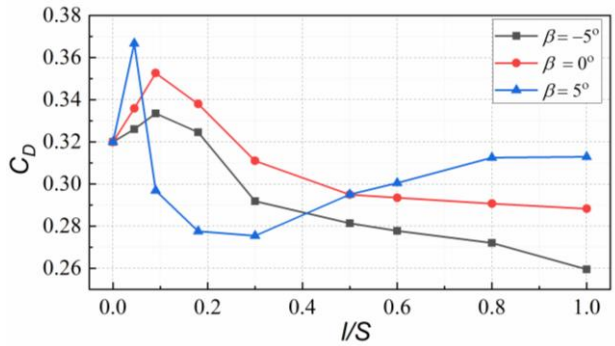

Figure 8. Aerodynamic force of the model

Previously, Tran et al. [11] showed that the angle with the minimum is approximately 0° for short deflector length from 4.5 to 18%. The angles with minimum drag are around -8° for long deflectors from 65% to 100% length of the slant, as noted by Kim et al. [1]. The selection of the -5° deflector is close to the optimization angle presented by Kim et al. [1] for long deflector lengths, where the longer length helps to reduce drag further. Additionally, the reducing drag obtained for both studies is similar at 18-19%. In terms of short deflector length, the angle with minimum drag is higher than the previous case by Tran et al. [11]. The different results are probably due to the effect of experimental setup and numerical methods. Previous studies applied the automatic lifting deflectors and the final angle could be affected by the weight of the deflector. Notably, the drag of the deflector angle of 5° for varied lengths shows a different trend to that of the two other configurations. Similar to the case of 9%, it is expected that the change of the drag is connected with a large modification of the flow structure around the slant. Detailed flow behavior relating to flow will be discussed in sections 3.3 and 3.4.

In the previous study, Tran et al. [35] demonstrated that the increasing drag for the model is mainly associated with increasing pressure drag acting on both the slant and the base. In the current study, we summarize the pressure drag generated on the slant $C_{Dp,\ slant}$ to understand its effect on the total drag. Results of $C_{Dp,\ slant}$ derived from the integrated pressure at the surface, for different deflector configurations,

are drawn in Figure 9. For the standard model, the pressure drag was $C_{Dp,\,slant}$=0.14. For the 5° deflector, the pressure drag of the slant rises with deflector angles of 4.5% at $C_{Dp,\,slant}$=0.16, then the drag decreases to a length of 30% and slightly increases with the length. For two other angles, $C_{Dp,\,the\,slant}$ is similar to the total drag. A slight difference in $C_{Dp,\,slant}$ for the case of 5° deflector at long-length deflectors in comparison to the total drag can be explained due to the generation of drag on the deflector and vertical base. Next, the flow phenomenon around the slant will be analyzed in more detail.

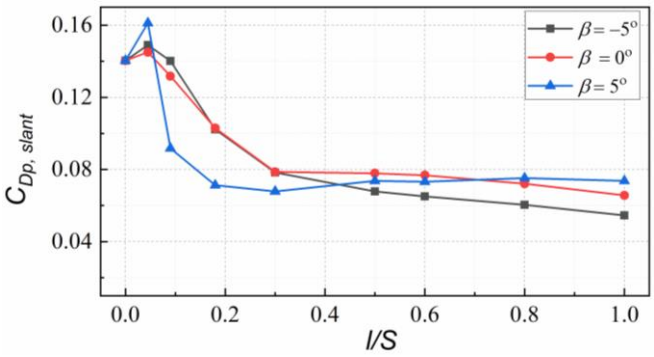

Figure 9. Pressure drag acting on the slant surface

3.3 Flow characteristics of the -5° deflector

Figure 10 presents the surface skin-friction streamlines superimposed on the pressure coefficient and the velocity on the symmetry plane for the -5° deflector at different lengths. It can be seen that the increasing drag with short deflector length is connected to a widening separation bubble. Additionally, even though the separation bubble is fully separated around the symmetric plane, the total drag is high because the steady structure of a separation bubble and two longitudinal vortices remain on the surface. The existence of those structures can be observed from the Q-criterion, as shown later in Figure 13. Additionally, the length of wake recirculation is less than 1.0*H* as shown in Figure 10(a), which is similar to that shown in Figure 7(d), (e). At *l*/*S*=30%, the flow is fully separated from the surface, featured by the corner vortex at the trailing edge and spreading to the whole spanwise direction of the slant. The convex flow occurs around the shoulder, which prevents the development of the wake flow in the vertical direction. In the gap between the model and deflector, the flow pattern is quite complicated. In the symmetry plane, the flow near the leading eddy shows a small recirculation region, which has a rotation direction similar to the corner vortex. Interestingly, this flow structure has small influences on the pressure at the surface. This is because the structure of the corner vortex is not large. The existence of corner vortices was reported in a previous investigation by Tran et al. [35]. This structure in the current study shows high consistency with the previous observation. However, the flow near the leading edge was not presented in the previous investigations due to the impact of deflectors on the measurement. Here, reduction in drag is associated with the formation and development of the corner vortex around the trailing edge, which is regular the flattened distribution of the pressure on the slant. This is an interesting physic phenomenon, which was not taken attention in previous studies. The presence of two vortices significantly diminishes the reversed flow above the slant [35]. The corner vortex develops over 0.5 lengths of the slant with reversed flow persisting in the remaining regions for the model with *l*/*S* = 80%. It should be noted that the RANS simulations often provide overpredicted results of the surface flow. By applying an improved turbulent model with parameter adjustment, highly accurate outcomes are achieved and presented.

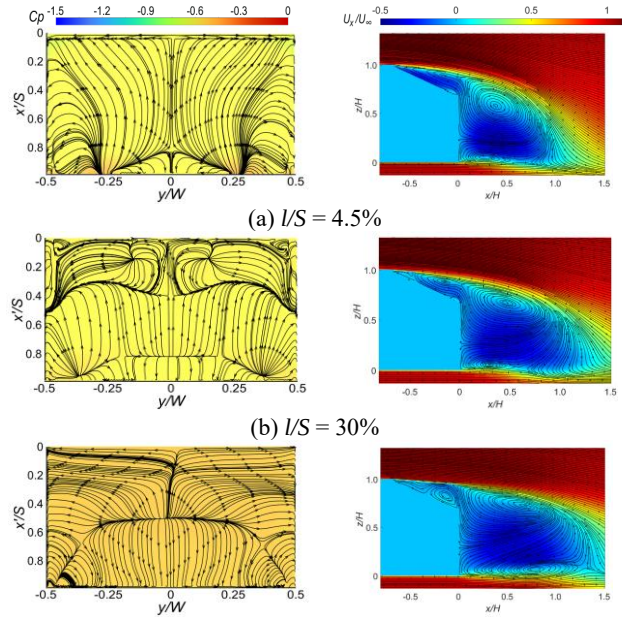

Figure 10. Skin-friction streamlines superimposed on pressure (left) and velocity on the vertical plane for -5° deflector

3.4 Flow characteristics of the 5° deflector

Next, the surface flow pattern and wake structure on the symmetry plane are discussed for the 5° deflector, where a high modification of the drag was generated. The results are shown in Figure 11. For the short deflector of 4.5%, a low-pressure area is formed on the slant connected to a large structure of the separation bubble and longitudinal vortices. Consequently, although the wake in the centerline is short, a high drag is generated for that configuration. As the deflector length increases to 30%, the fully separated flow occurs, pressure distribution becomes flat and the drag of the model decreases. For a long deflector length of *l*/*S* = 80%, the skin-friction structure is similar to other cases with a reversed flow region in the midpoint of the slant and a corner vortex around the trailing edge. It can be confirmed that the corner vortex is generated due to the interaction of the slant and deflector plate. The corner vortex becomes large, which reaches 70% of the total length of the slant. The simulation indicates that small longitudinal vortices are probably generated around the edges. This structure will be discussed by the Q-criterion in section 3.6. The streamlines of the velocity also indicate that the upper vortex of the wake moves upward. As a result, the concave flow fields occur near the leading edge, which results in an expansion of the wake structure in the vertical direction and movement upward of the upper vortices. This flow field is different for other cases and is the reason for the increasing drag [36].

3.5 Flow on the cross-sectional plane

Figure 12 presents the streamlines mixing with velocity fields on a cross-sectional plane (*x*=0.22 m) behind the base for different flap angles. The loss of the velocity presents

relatively the drag of the model. The coherence of the longitudinal vortices is identified for the standard model. At 5° deflector and length of 4.5%, the vortices become stronger. However, for longer lengths at 30%, the vortices are less coherent. Additionally, the merge of the longitudinal vortex with the main separation flow to form a large wake can be observed from the velocity loss on the cross-sectional plane. The effect of the longitudinal vortices on pressure at the slant and total drag becomes less for fully separated flow. As the deflector angle increases further, the wake flow becomes wider. As a result, the drag coefficient increases. The numerical results are in agreement well to previous experimental and numerical data. A slight departure from experimental results is probably due to the different setup and experimental process.

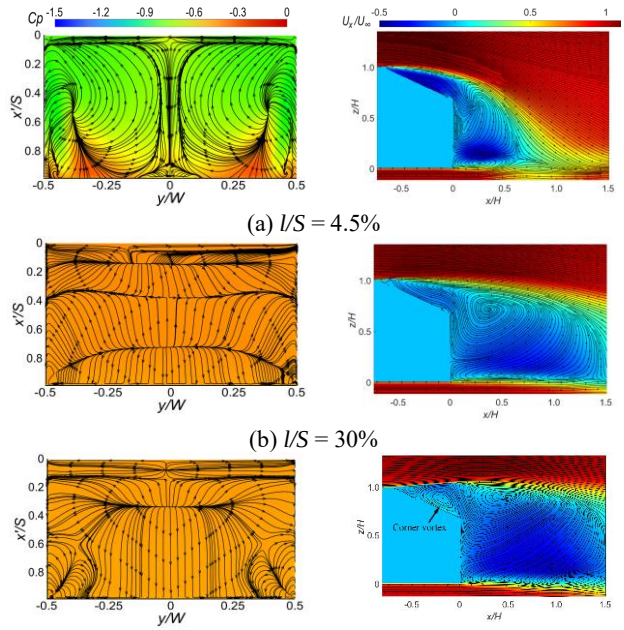

(a) l/S = 4.5%

(b) l/S = 30%

(c) l/S = 80%

Figure 11. Skin-friction lines superimposed on pressure (left) and velocity on the vertical plane for 5° deflector

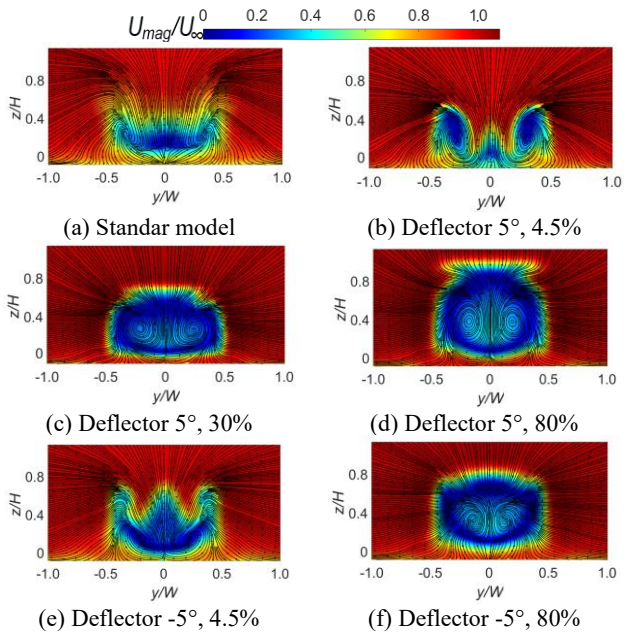

(a) Standar model

(b) Deflector 5°, 4.5%

(c) Deflector 5°, 30%

(d) Deflector 5°, 80%

(e) Deflector -5°, 4.5%

(f) Deflector -5°, 80%

Figure 12. Streamlines superimposed to streamwise velocity on the symmetry plane

3.6 Wake flow at different deflectors

For more details of the wake structure, Figure 13 presents the Q-criterion of the velocity invariant with a value of 18000. The results of Q-criterion show a high effective method for visualizing the main structure of the wake flow. Here, a separation bubble and two longitudinal vortices above the slant are presented for the standard case, along with a ring shape of the recirculation vortex behind the base. Stronger longitudinal vortices and larger longitudinal vortices are generated for the model with 5° and 4.5% length deflector. Increasing deflector length leads to the breakdown of this structure as shown in Figure 13(c) for the case of 5° and 30% length deflector. Here, the wake flow is formed by a small vortex structure, and no dominant large-scale features are observed. It seems that the longitudinal vortices are formed again above the slant for 80% deflector as shown in Figure 13(d). Interestingly, longitudinal vortices are also generated at the lower surface of the deflector. The existence of two vortices can be observed clearly from two tornados downstream of the base. A C-type vortex is also generated near the base, which explains for high turbulent intensity shown later in Figure 14. A similar pattern is obtained for the case of the -5° deflector for short deflector length. The difference here is that at the 80% length deflectors (Figure 13(f)), two longitudinal vortices are formed above the slant and also above the deflector, which is different for the case of the 5°deflector, where only a pair of longitudinal vortices occur in two side of the slant. Additionally, although the C-type vortex is closer to the base, it is weaker than that of the 5° deflector model. The movement of the longitudinal vortices changes the pressure distribution on the slant surface and thereby the drag of the model.

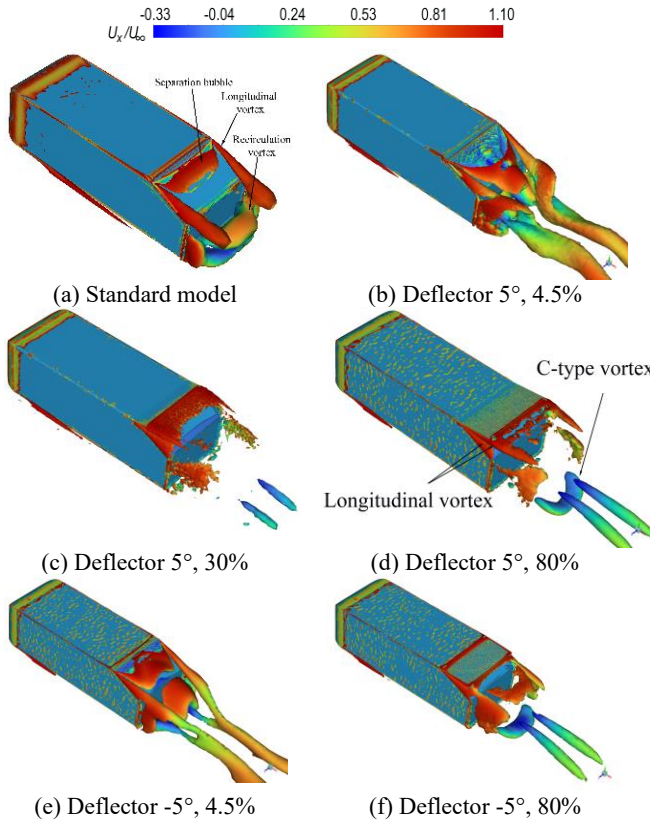

(a) Standard model

(b) Deflector 5°, 4.5%

(c) Deflector 5°, 30%

(d) Deflector 5°, 80%

(e) Deflector -5°, 4.5%

(f) Deflector -5°, 80%

Figure 13. Vortex structured around the model illustrated by iso-surface of Q-criterions

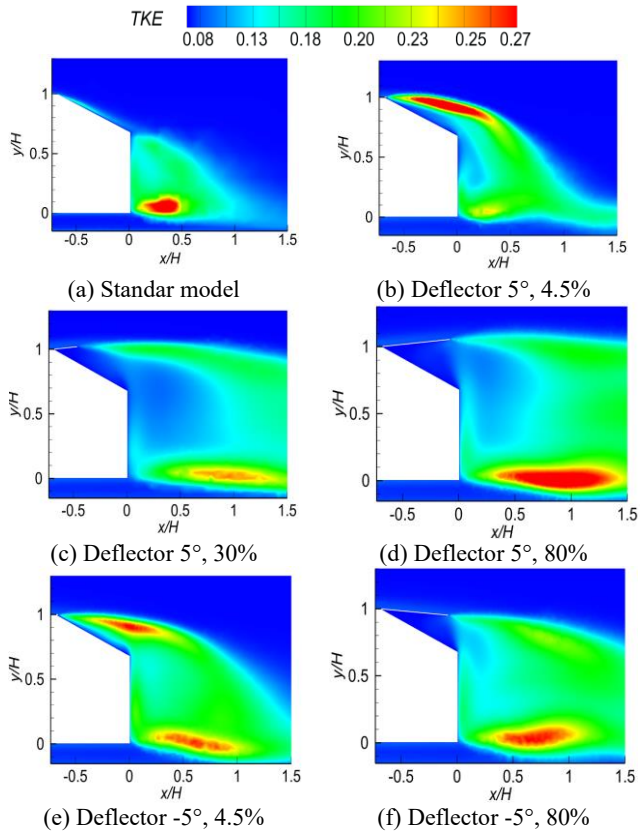

Figure 14. TKE k on the symmetry plane $y/W = 0$

3.7 Turbulent kinetic energy (TKE)

Figure 14 presents the TKE in the wake region for different deflection configurations. The results of TKE help explain the turbulent mixing of the wake flow. For the standard model, the maximum TKE of around 0.27 occurs at the bottom vortex center. These results are consistent with the previous observation by Tunay et al. [39], who utilized two-component particle image velocimetry to measure the flow on symmetry planes for different slant angles. In the present study, the maximum turbulent kinetic energy (TKE) reaches approximately 0.27 for the standard model, slightly surpassing the value of 0.24 observed in the previous study. This discrepancy can be attributed to the fact that in the current investigation, TKE is calculated by three components of the velocity while two components were calculated previously. The maximum TKE moves above the upper surface of the slant for the 5° deflector with a length of 4.5%. The elevated turbulent kinetic energy (TKE) accounts for the low-pressure area on the slant, as depicted in Figure 11(a). An analogous distribution of TKE occurs for -5° and 4.5% deflector. However, for that configuration, high TKE is also observed at the bottom vortex. Interestingly, the decrease of the drag for 30° and 30% deflector is connected to low maximum TKE in comparison to other models. For the 5° deflector with 80% length, the high aerodynamic drag is connected to a long high TKE at the bottom. The high TKE at the cases of 4.5% and 80% for 5° deflector explained for the increase drag in comparison to the baseline case as shown in Figure 8. The outcomes of the present study confirm the presence of two states associated with high drag regimes. The first stage is connected to a large structure on the slant. The second stage is connected to large wake structures in horizontal and vertical directions and high turbulent TKE.

4. CONCLUSIONS

Aerodynamic drag and flow behavior around the Ahmed body equipped with deflectors were presented. The deflector angles were kept constant, while their length varied from 0 to 1S, aiming to comprehend their impact on the flow structure and the drag tendency. A numerical simulation based on the generalized GEKO turbulent model with parameter adjustments was applied to analyze the complex flow. The coefficient C_{sep}=2.5 provides good results of surface flow and drag coefficient. The results indicate that the current method shows a good ability to predict flow behavior around the model with clear surface skin-friction fields and drag. This numerical result was first successfully obtained in this study for 25° Ahmed body by RANS simulation. The primary conclusion drawn from the study is as follows:

The deflectors prove to be an efficient mechanism for diminishing the aerodynamic drag of the 25° Ahmed body. A maximum reducing drag was observed at 19% for flap angles of -5° and lengths of 1.0S, which was firstly presented in the current study.

The reduction in drag is associated with the disruption of the separation bubble and longitudinal vortices on the surface and the reduction of TKE behind the model. The flow structure for the low drag regime is featured by corner vortices above the slant and concave velocity fields around the leading edge.

For -5° and 0° deflectors, there is a greater degree of drag reduction with increasing deflector length, aligning with earlier findings reported by Kim et al. [1] and Tran et al. [35]. However, the drag tendency for a 5° deflector angle indicates a minimum value at l/S = 30%, which is not presented previously. The reduction of drag at this configuration is approximately 14%.

The high drag region is connected to two types of wake flows: The first flow type is characterized by a large separation bubble above the slant and strong longitudinal vortices near two side edges. The second flow type is featured by a large wake with concave flow fields around the leading edge and high TKE in the wake region. The mechanism of second flow types with high drag was firstly presented in the current study. The Q-criterion presents that the longitudinal vortex is formed again above the slant and below the deflector for this type of flow.

Although the current RANS simulation provides highly accurate results of averaged surface flow and drag trend, higher numerical schemes, for example, detached eddy simulation and large eddy simulation, should be conducted for the simulation to understand the unsteady aerodynamics of the model with deflectors. It is an important task for our further studies.

ACKNOWLEDGMENT

Pham Van Duy was funded by the Master, PhD Scholarship Program of Vingroup Innovation Foundation (VINIF), code VINIF.2023.ThS.026.

REFERENCES

[1] Kim, D., Lee, H., Yi, W., Choi, H. (2016). A bio-inspired device for drag reduction on a three-dimensional model vehicle. Bioinspiration and Biomimetics, 11(2): 026004.

https://doi.org/10.1088/1748-3190/11/2/026004
[2] Ahmed, S.R., Ramm, G., Faltin, G. (1984). Some salient features of the time - averaged ground. SAE Transactions, 93(2): 473-503. https://doi.org/10.4271/840300
[3] Perry, A.K., Pavia, G., Passmore, M. (2016). Influence of short rear end tapers on the wake of a simplified square-back vehicle: Wake topology and rear drag. Experiments in Fluids, 57(11): 169. https://doi.org/10.1007/s00348-016-2260-3
[4] Irving Brown, Y.A., Windsor, S., Gaylard, A.P. (2010). The effect of base bleed and rear cavities on the drag of an SUV. SAE Technical Papers 2010-01-0512. https://doi.org/10.4271/2010-01-0512
[5] Meile, W., Brenn, G., Reppenhagen, A., Lechner, B., F.A. (2011). Experiments and numerical simulations on the aerodynamics of the Ahmed body. CFD Letters 3(1): 32-39.
[6] Le, A.D., Phan Thanh, H., Tran The, H. (2021). Assessment of a homogeneous model for simulating a cavitating flow in water under a wide range of temperatures. Journal of Fluids Engineering, 143(10): 101204. https://doi.org/10.1115/1.4051078
[7] Tran, T.H., Anyoji, M., Nakashima, T., Shimizu, K., Le, A.D. (2022). Experimental study of the skin-friction topology around the Ahmed body in cross-wind conditions. Journal of Fluids Engineering, 144(3): 031209. https://doi.org/10.1115/1.4052418
[8] Beaudoin, J.F., Aider, J.L. (2005). Drag and lift reduction of a 3D bluff body using flaps. Experiments in Fluids, 44(4): 491-501. https://doi.org/10.1007/s00348-007-0392-1
[9] Fourrie, G., Keirsbulck, L., Labraga, L., Gilliéron, P. (2011). Bluff-body drag reduction using a deflector. Experiments in Fluids 50(2): 385-395. https://doi.org/10.1007/s00348-010-0937-6
[10] Wang, H.F., Zhou, Y., Zou, C., He, X.H. (2016). Aerodynamic drag reduction of an ahmed body based on deflectors. Journal of Wind Engineering and Industrial Aerodynamics, 148: 34-44. https://doi.org/10.1016/j.jweia.2015.11.004
[11] Tran, T.H., Hijikuro, M., Anyoji, M., Uchida, T., Nakashima, T., Shimizu, K. (2023). Effect of a short, bio-mimetic control device on aerodynamic drag of Ahmed body. Journal of Fluids Engineering, 145(3): e031206. https://doi.org/10.1115/1.4056341
[12] Tian, J., Zhang, Y., Zhu, H., Xiao, H. (2017). Aerodynamic drag reduction and flow control of Ahmed body with flaps. Advances in Mechanical Engineering, 9(7): 1-17. https://doi.org/10.1177/1687814017711390
[13] Raina, A., Harmain, G.A., Haq, M.I.U. (2017). Numerical investigation of flow around a 3D bluff body using deflector plate. International Journal of Mechanical Sciences, 131-132: 701-711. https://doi.org/10.1016/j.ijmecsci.2017.08.018
[14] Cheng, S.Y., Chin, K.Y., Mansor, S., Abd Rahman, A.B. (2018). Experimental study of yaw angle effect on the aerodynamic characteristics of a road vehicle fitted with a rear spoiler. Journal of Wind Engineering and Industrial Aerodynamics, 184(12): 305-312. https://doi.org/10.1016/j.jweia.2018.11.033
[15] Kamaci, C., Kaya, K. (2021). Numerical investigation of aerodynamic properties of Ahmed body for different rear slanted surface configurations. European Journal of Science and Technology, 28: 469-475. https://doi.org/10.31590/ejosat.1005846
[16] Siddiqui, N.A., Chaab, M.A. (2020). A simple passive device for the drag reduction of an Ahmed body. Journal of Applied Fluid Mechanics, 14(1): 147-164. https://doi.org/10.47176/jafm.14.01.31791
[17] Maine, M., Oumami, M.E., Bouksour, O., Nassiri, B. (2021). Study of the effect of some deflector's geometry factors on the reduction of the aerodynamic drag of the car model. Jordan Journal of Mechanical and Industrial Engineering, 15(3): 265-272.
[18] Tran, T.H., Hijikuro, M., Anyoji, M., Uchida, T., Nakashima, T., Shimizu, K. (2023). Surface flow and aerodynamic drag of Ahmed body with deflectors. Experimental Thermal and Fluid Science, 145: e110887. https://doi.org/10.1016/j.expthermflusci.2023.110887
[19] Le, A.D., Minh, B., Hoang Van, T., The Hung, T. (2022). Modified Savonius wind turbine for wind energy harvesting in urban environments. Journal of Fluids Engineering, 144(8): 081501. https://doi.org/10.1115/1.4053619
[20] Duc, M.B., The, H.T., Van, K.P., Le, A.D. (2023). Predicting aerodynamic performance of Savonius wind turbine: An application of generalized k-ω turbulence model. Ocean Engineering, 286: e115690. https://doi.org/10.1016/j.oceaneng.2023.115690
[21] Shabarov, V., Kalyasov, P., Shaposhnikov, V., Peplin, F. (2021). Method of unsteady hydrodynamic characteristics determination in turbulent boundary layer. Journal of Applied and Computational Mechanics, 7(2): 849-857. https://doi.org/10.22055/JACM.2020.34992.2534
[22] Abikan, A., Yang, Z., Lu, Y. (2020). Computational analysis of turbulent flow over a bluff body with drag reduction devices. Journal of Applied and Computational Mechanics, 6: 1210-1219. https://doi.org/10.22055/JACM.2020.32667.2055
[23] Viswanathan, H. (2021). Aerodynamic performance of several passive vortex generator configurations on an Ahmed body subjected to yaw angles. Journal of the Brazilian Society of Mechanical Sciences and Engineering, 43(3): 131. https://doi.org/10.1007/s40430-021-02850-8
[24] Zhou, H., Chen, Q., Qin, R., Zhang, L., Li, H. (2021). Investigation of wheelhouse shapes on the aerodynamic characteristics of a generic car model. Advances in Mechanical Engineering, 13(12): 1-13. https://doi.org/10.1177/16878140211066842
[25] Guilmineau, E. (2008). Computational study of flow around a simplified car body. Journal of Wind Engineering and Industrial Aerodynamics, 96(6-7): 1207-1217. https://doi.org/10.1016/j.jweia.2007.06.041
[26] Ashton, N., Revell, A. (2005). Key factors in the use of DDES for the flow around a simplified car. International Journal of Heat and Fluid Flow, 54: 236-249. https://doi.org/10.1016/j.ijheatfluidflow.2015.06.002
[27] Kapadia, S., Roy, S., Wurtzler, K. (2003). Detached eddy simulation over a reference ahmed car model. In 41st Aerospace Sciences Meeting and Exhibit, Reno, Nevada, pp. 481-488. https://doi.org/10.2514/6.2003-857
[28] Guilmineau, E., Deng, G. B., Leroyer, A., Queutey, P., Visonneau, M., Wackers, J. (2018). Assessment of hybrid RANS-LES formulations for flow simulation around the Ahmed body. Computers and Fluids, 176(1): 302-319.

https://doi.org/10.1016/j.compfluid.2017.01.005
[29] Delassaux, F., Mortazavi, I., Itam, E., Herbert, V., Ribes, C. (2021). Sensitivity analysis of hybrid methods for the flow around the Ahmed body with application to passive control with rounded edges. Computers and Fluids, 214: e104757. https://doi.org/10.1016/j.compfluid.2020.104757
[30] Krajnović, S., Davidson, L. (2005). Flow around a simplified car, part 1: Large eddy simulation. Journal of Fluids Engineering, Transactions of the ASME, 125(5): 907-918. https://doi.org/10.1115/1.1989371
[31] Serre, E., Minguez, M., Pasquetti, R., Guilmineau, E., Deng, G.B., Kornhaas, M., Schäfer, M., Fröhlich, J., Hinterberger, C., Rodi, W. (2013). On simulating the turbulent flow around the Ahmed body: A french-german collaborative evaluation of LES and DES. Computers and Fluids, 78: 10-23. https://doi.org/10.1016/j.compfluid.2011.05.017
[32] Minguez, M., Pasquetti, R., Serre, E. (2008). High-order large-eddy simulation of flow over the "Ahmed body" car model. Physics of Fluids, 20(9): 095101. https://doi.org/10.1063/1.2952595
[33] Heft, A.I., Indinger, T. Adams, N.A. (2011). Investigation of unsteady flow structures in the wake of a realistic generic car model. In 29th AIAA Applied Aerodynamics Conference, pp. 1-14. https://doi.org/10.2514/6.2011-3669
[34] Fares, E. (2006). Unsteady flow simulation of the Ahmed reference body using a lattice Boltzmann approach. Computers and Fluids, 35(8-9): 940-950. https://doi.org/10.1016/j.compfluid.2005.04.011
[35] Tran, T.H., Hijikuro, M., Anyoji, M., Uchida, T., Nakashima, T., Shimizu, K. (2022). Deflector effect on flow behavior and drag of an Ahmed body under crosswind conditions. Journal of Wind Engineering and Industrial Aerodynamics, 231(8-9): e105238. https://doi.org/10.1016/j.jweia.2022.105238
[36] Siddiqui, N.A., Agelin-Chaab, M. (2022). Flow features of the Ahmed body at a low Reynolds number. International Journal of Heat and Fluid Flow, 98: e109052. https://doi.org/10.1016/j.ijheatfluidflow.2022.109052
[37] Menter, F.R., Lechner, R., Matyushenko, A. (2019). Best practice: Generalized k-ω two-equation turbulence model in ANSYS CFD (GEKO). ANSYS Germany GmbH.
[38] Mestiri, R., Ahmed-Bensoltane, A., Keirsbulck, L., Aloui, F., Labraga, L. (2014). Active flow control at the rear end of a generic car model using steady blowing. Journal of Applied Fluid Mechanics, 7(4): 565-571. https://doi.org/10.36884/jafm.7.04.21752
[39] Tunay, T., Sahin, B., Ozbolat, V. (2014). Effects of rear slant angles on the flow characteristics of Ahmed body. Experimental Thermal and Fluid Science, 57: 165-176. https://doi.org/10.1016/j.expthermflusci.2014.04.016

NOMENCLATURE

C_D	drag coefficient
$C_{Dp,\ slant}$	pressure drag on the slant
Cp	pressure coefficient
$RANS$	Reynolds averaged Navier-stokes
Re_H	Reynolds number by height
TKE	turbulent kinetic energy

Greek symbols

θ	deflector angle [º]